GENERAL PHYSICS

I. RADIO ASTRONOMY

Academic and Research Staff

Prof. A. H. Barrett
Prof. B. F. Burke
Prof. Susan G. Kleinmann
Prof. R. M. Price
Prof. D. H. Staelin
Dr. P. L. Kebabian
Dr. K. F. Kunzi
Dr. P. C. Myers
Dr. G. D. Papadopoulos
Dr. J. Sander
Dr. J. W. Waters
J. W. Barrett
D. C. Papa

Graduate Students

B. G. Anderson
O. Appiah
K. P. Bechis
W. G. Brodsky
P. C. Crane
R. W. Freund
T. S. Giuffrida
A. D. Haschick
P. Ho
K-S. Lam
K-Y. Lo
R. N. Martin
R. W. McGahan
R. L. Pettyjohn
R. K. L. Poon
J. H. Spencer
R. C. Walker
T. J. Warren
R. W. Wilcox

A. MICROWAVE SENSING OF SUBCUTANEOUS TEMPERATURES

Joint Services Electronics Program (Contract DAAB07-71-C-0300)

P. C. Myers, A. H. Barrett

Since our first report on the investigation of microwave radiometry as a medical diagnostic technique[1] work has progressed in measurement technique, equipment development, and preparation for clinical tests. In this report, we present results of our first measurements, which indicate the feasibility of detecting subcutaneous temperature elevation with a microwave radiometer under controlled conditions. These measurements, which were completed in September 1972, are quite crude in the light of our present and anticipated measurement capabilities. We then discuss engineering and design work, most of which has been completed. Finally, we mention briefly the opportunities for clinical tests which we are now exploring with doctors in nearby hospitals.

1. Initial Measurements of Subcutaneous Temperature Elevation

In September 1972, with the assistance of P. P. Lele and W. Hsu in the Laboratory of Experimental Medicine, we conducted temperature measurements of necrotic muscle tissue of the cat thigh. A local temperature elevation was produced in the muscle by directing a focused beam of ultrasonic power into the muscle through an appropriate coupling medium. This technique has been described by Lele.[2] The temperature distribution in the muscle tissue was monitored by a chromel-constantan thermocouple of 0.005 in. diameter, which had been implanted in the muscle through the bore of a hollow steel tube. The tube was removed before the temperature measurements were begun. The thermocouple wire was rigidly attached to a micromanipulator, so that the thermocouple junction could be scanned along a line through the muscle tissue. The cat

skin-surface temperature was measured with a thermistor thermometer whose sensing element was in thermal contact with a metal disk, 1 cm in diameter. Microwave sensing of the subsurface temperature was provided by a dielectric-filled waveguide antenna and a 3-GHz radiometer which have been described previously.[1] The antenna aperture was placed in contact with the skin surface. The temperature elevation sensed by the antenna and radiometer was located in the near radiation field of the antenna; hence, its spatial resolution was approximately equal to the cross section of the aperture (1.0 × 2.3 cm).

Figure I-1 shows the response of the implanted thermocouple and microwave radiometer to ultrasonic heating of the muscle tissue as a function of time. The thermocouple junction and microwave antenna were each kept at one position during the entire measurement. The thermocouple junction was located at the peak of the internal temperature

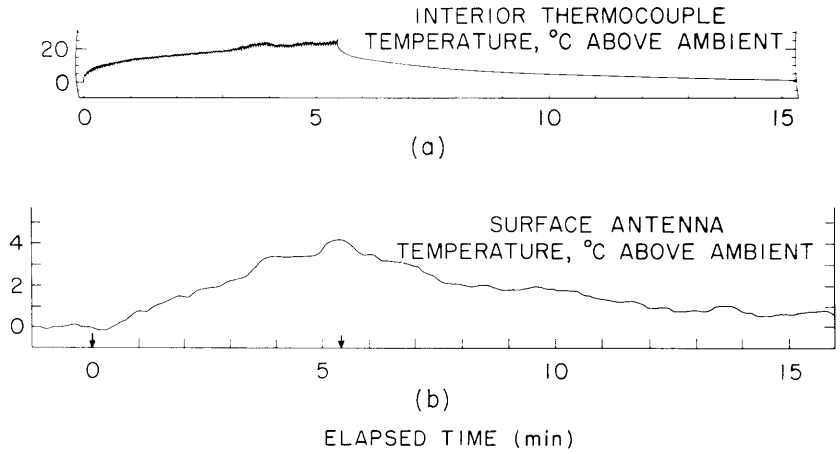

Fig. I-1. Time history of (a) temperature of dead cat thigh muscle, heated with pulsed focused ultrasound, measured with a thermocouple implanted at the focus approximately 1.5 cm beneath the skin surface, and (b) temperature recorded by a 3-GHz microwave radiometer, with antenna fixed against the skin surface. Arrows indicate beginning and end of the ultrasonic irradiation period.

distribution. The microwave antenna was placed with its aperture flush against the skin surface. The aperture was ~1.5 cm from the center of the heated region measured along the antenna axis. The axis was horizontal; the ultrasonic beam was incident from above. The rapid rise in interior temperature in Fig. I-1a indicates the onset of ultrasonic irradiation; this point is shown by an arrow in Fig. I-1b. The pulses in (a) reflect the pulsed nature of the incident ultrasound. The microwave record does not show this structure because the radiometer time constant (10 s) was much longer than the pulse period. The ultrasonic heating was stopped after 5.5 min; this point is evident in (a) and is indicated by an arrow in (b). The amplitude of the microwave radiometer response is less than

the amplitude of the thermocouple response because of radiation absorption by the muscle tissue and because the extent of the heated region is smaller than the spatial response pattern of the antenna.

Figure I-2 shows 3 scans across a region of temperature elevation whose intensity and extent are nearly constant during the period of measurement. The implanted thermocouple junction was drawn away from the position of peak temperature in 3-mm steps by

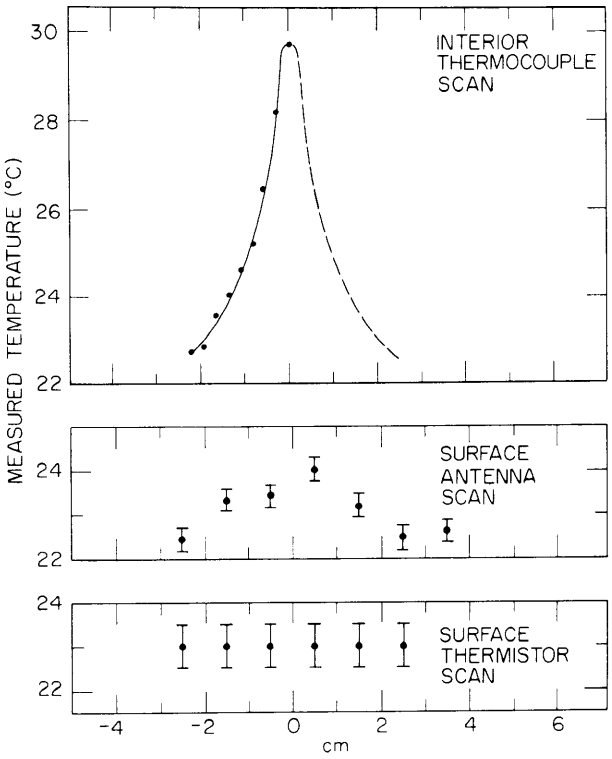

Fig. I-2. Temperature scans across ultrasonically heated dead cat muscle. The dashed portion of the upper curve is extrapolated. The middle scan shows the microwave radiometer response. Bars indicate peak-to-peak errors.

the micromanipulator; the result of this scan is shown in the upper curve. The center curve shows the result of a scan of the microwave antenna across the skin. The shortest distance between the scan line and hot-spot center was approximately 1 cm. The error bars indicate peak-to-peak noise fluctuations about the mean antenna temperature measured at each location. The microwave record shows a clear rise and fall as the antenna pattern passes through the hot region. But, a scan across the same surface region with the thermistor thermometer, shown in the lower curve, has no corresponding peak. This indicates a microwave capability of detecting a subsurface temperature anomaly that

might not be detected by a surface-temperature measurement.

These data were taken with instruments and techniques that have since been substantially improved. We intend to repeat and extend these measurements, as soon as our initial equipment upgrading is completed. In particular, we plan to perform these measurements on living cat tissue, so that the circulating blood can modify the thermal distribution caused by ultrasonic heating. The thermal distribution will then be more complex, but also more realistic in its similarity to the thermal distribution caused by a tumor.

A program is under way to study the thermal distribution of a developing abscess as a function of position and time in cat muscle. We expect to carry out a similar study of malignant tumor growth, using laboratory animals. This study should serve as a useful complement to clinical examinations, which we hope to begin within 6 months.

2. Development and Design Work

Our primary effort has been to repackage our 3-GHz radiometer in a rack-mounting box which provides adequate shielding and filtering against interfering signals, particularly in the intermediate-frequency range (10-110 MHz). This work is now completed; the repackaged radiometer is being tested and its performance optimized for its new configuration. Shielding is provided by a welded aluminum box, $5 \times 17 \times 17$ in., with walls 1/8 in. thick and a cover plate whose underside is coated with a metal-braid shielding gasket. The radiometer box is attached with screws and side brackets to a 10.5×19 in. rack-mounting panel which provides appropriate input ports, control switches, and monitor ports and meters for control and monitoring of the radiometer performance. Direct current power is supplied to the box from another rack-mounting unit through a shielded connector, with a filter on each power line typically giving 20 dB rejection of pickup across the 10-110 MHz band. We have gone to some lengths to shield the radiometer in this manner because of the variety of communication and noiselike signals in the 10-110 MHz band in a typical hospital environment. We expect to package our 1-GHz radiometer in a similar way.

Assembly and testing are now completed on a bridge circuit with two thermistor probe inputs and a meter display. Calibration tests indicate a temperature sensitivity of better than 0.2°K (peak-to-peak error) across the range 15°C to 50°C with an e^{-1} response time of approximately 10 seconds. The thermistor probe is a disk of 3/8 in. diameter with a metal face to contact the area to be sensed and an obverse face of low thermal conductivity. The probe is attached to one face of a small box which can be mounted on the microwave antenna. In this way application of the microwave antenna to the skin will also provide a thermistor indication of the surface temperature from a disk of skin approximately 1 cm from the antenna aperture. A two-dimensional grid of microwave observations will thus give a two-dimensional grid of surface measurements, which

will overlap the microwave grid except for two bands that are 1 cm wide. We expect that comparison of the two types of thermal pattern may provide some useful information.

In preparing the direct-contact probe we have sought to quantify the effect of the measurement process on the temperatures that are being measured. Thermal conduction by the probe and pressure of the probe against the skin can cause variations in the measured surface temperature and possibly also in the microwave antenna temperature. We are investigating the magnitude of these effects and experimenting with various types of thin, flexible, air-filled foam of low thermal conductivity to serve as a skin-antenna interface.

Work continues on impedance matching of our antennas at 3 GHz and 1 GHz to the 50 Ω radiometer input impedance by use of $\lambda/4$ coaxial impedance transformers.

We are placing a major effort on digital data handling, storage, and display. Our data presentation goal is a real-time two-dimensional display of temperature, similar to that obtained with the infrared thermograph but with much coarser resolution. We also intend to produce a real-time hard-copy record of this temperature map, and may want to record the data on magnetic tape for additional post real-time processing. Additional data-handling features may become desirable as we become more familiar with the nature of the data and the data-taking process. As a first step toward this goal we have completed the design and begun construction of a digital control and display unit. This unit will periodically receive and store radiometer calibration data, and use these data to provide a real-time L. E. D. numeral display of sensed microwave temperature difference. It will also permit monitoring of variations in the radiometer gain and output level. The design of this unit provides several data-handling options, in order to give maximum compatibility with the larger digital display and control system which will follow.

3. Opportunities for Clinical Tests

We have begun to explore the prospect of collaboration with clinicians and radiologists who examine patients with possible thermal anomalies.

Our main clinical testing interest is in using microwave and infrared thermographs, and possibly an x-ray device (mammograph or Xerograph) to examine a significant number of patients with suspected breast tumors. Comparison of detection statistics should indicate the relative utility of microwave thermography for this application. Doctors with whom we have discussed this project are enthusiastic, and we are considering offers of collaboration from physicians affiliated with the M. I. T. High Voltage Laboratory, Boston Hospital for Women, and Faulkner Hospital. Our conversations with these doctors have suggested many other potential clinical applications of microwave thermography which we plan to explore as part of our testing program.

We wish to thank J. W. Barrett, G. Bolen, L. Bromberg, D. Deacon, P. Ho, W. Hsu, G. Langlais, A. Lazzarini, P. P. Lele, and D. C. Papa for advice and technical assistance.

References

1. A. H. Barrett and P. C. Myers, Quarterly Progress Report No. 107, Research Laboratory of Electronics, M.I.T., October 15, 1972, pp. 14-18.

2. P. P. Lele, J. Physiol. 160, 494 (1962).

B. PRELIMINARY RESULTS FROM THE NIMBUS-5 MICROWAVE SPECTROMETER EXPERIMENT

California Institute of Technology (Contract 952568)

D. H. Staelin, F. T. Barath, A. H. Barrett, N. E. Gaut, K. F. Kunzi, W. B. Lenoir, W. Nordberg, R. L. Pettyjohn, R. K. L. Poon, P. W. Rosenkranz, J. W. Waters, R. W. Wilcox

[F. T. Barath and P. W. Rosenkranz are at the California Institute of Technology Jet Propulsion Laboratory. N. E. Gaut is at Environmental Research and Technology, Inc. W. Nordberg is at Goddard Space Flight Center.]

The Nimbus-5 Microwave Spectrometer Experiment (NEMS) is the first step in the application of the microwave spectrum to global sensing of atmospheric temperature structure. The instrument also yields unique information about the atmospheric humidity and cloud water content over oceans, and about such parameters as snow cover, ice type, soil moisture, sea state, and so forth. The instrument views the nadir continuously

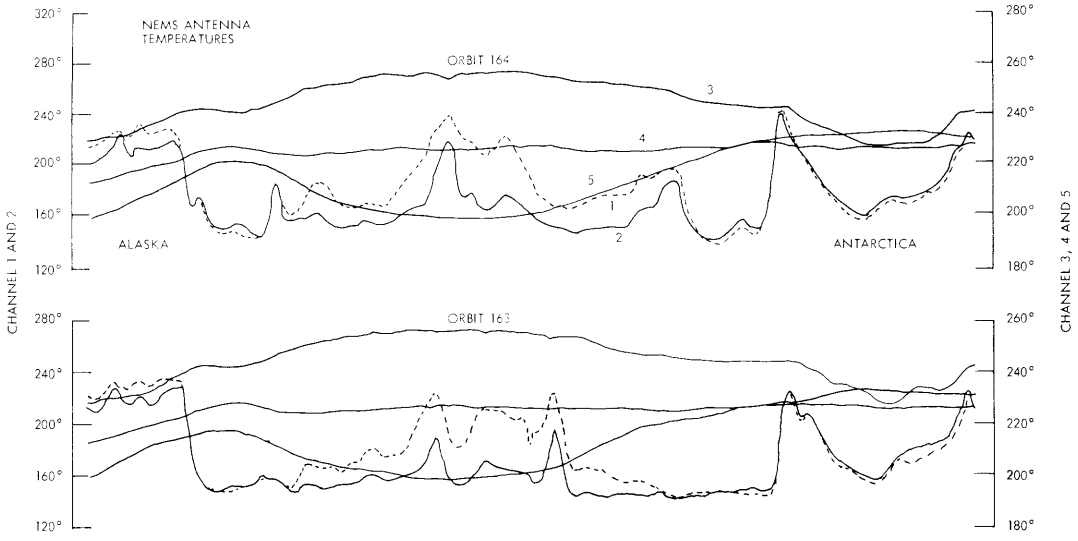

Fig. I-3. Observed antenna temperatures (°K) for orbits 163 and 164. The orbits pass from Alaska to Antarctica across the Pacific Ocean.

with a spatial resolution of ~170 km, and measures the thermal radiation at 22.235, 31.4, 53.65, 54.9, and 58.8 GHz with a sensitivity of ~0.1-0.2°K for 16-s integration. Since launch on December 11, 1972, the instrument has operated continuously without apparent difficulty or degradation.

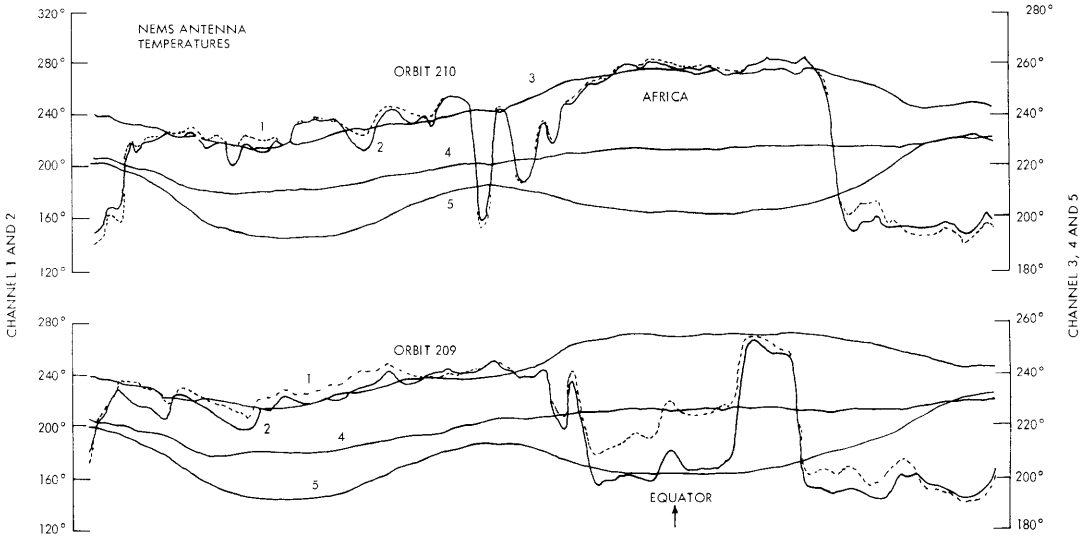

Fig. I-4. Observed antenna temperatures (°K) for orbits 209 and 210. The orbits pass from northern Asia toward Antarctica across Madagascar (orbit 209) and Africa (orbit 210).

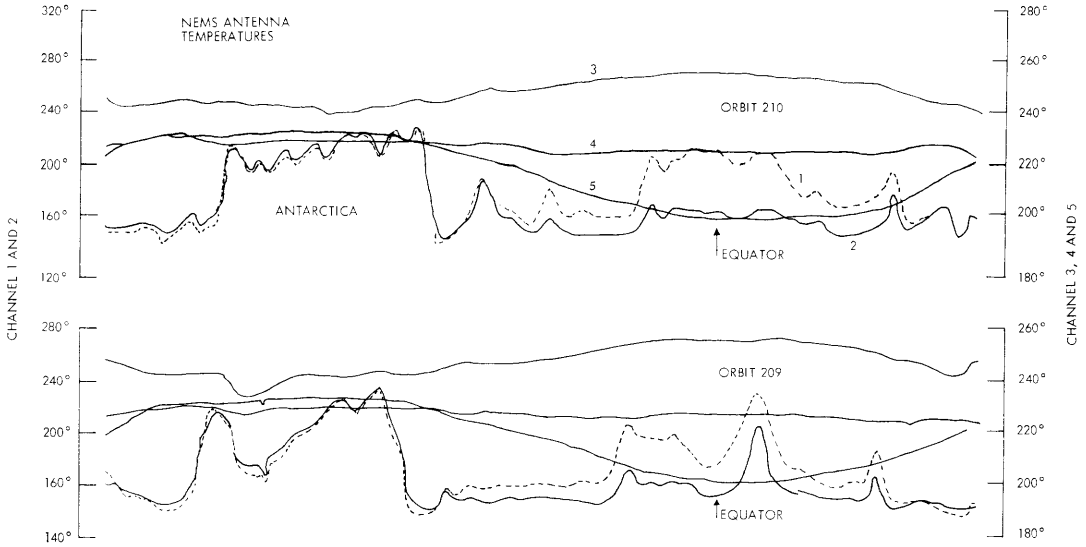

Fig. I-5. Observed antenna temperatures (°K) for orbits 209 and 210. The orbits pass across Antarctica and northward across the Pacific Ocean.

In Figures I-3, I-4, and I-5 antenna temperatures (radiances) are plotted for several orbits. Channels 1-5 are numbered in order of increasing frequency. Orbits 163 and 164, shown in Fig. I-3, illustrate several phenomena. For example, the arctic and antarctic are evident as high-temperature regions in channels 1 and 2. Two unexpected phenomena are evident in the arctic regions. First, the center of the antarctic radiates remarkably little microwave energy in channels 1 and 2; the antenna temperatures are approximately 160°K, far colder than the arctic sea ice, and second, the spectral properties of the arctic sea ice and the inland antarctic ice are different. In the arctic, channel 2 is uniformly colder than channel 1, whereas in the antarctic the temperature of the channels is reversed. The ice in central Greenland resembles that of central Antarctica. These spectral properties, which vary from place to place, should provide new information about the distribution of various types of ice.

In the center of Fig. I-3 the humid tropical regions over the Pacific Ocean are evident. The integrated water-vapor density over ocean is approximately proportional to the spread between channels 1 and 2. The liquid water content is approximately proportional to the displacement of channel 2 from Arctic Ocean values. The intertropical convergence (ITC) zone is marked by strong rain bands and high humidity, and is plainly evident near the equator.

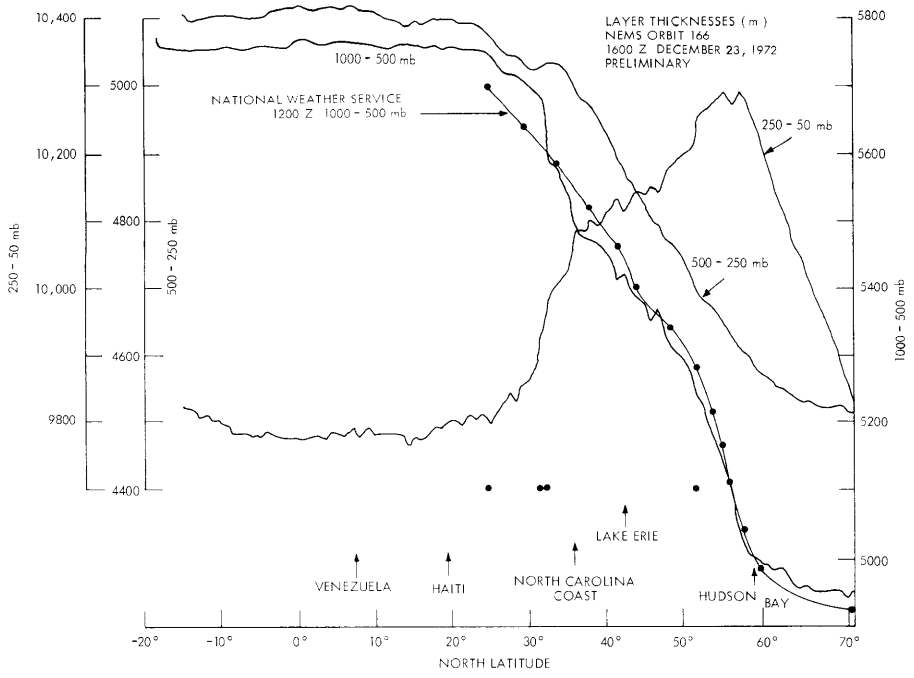

Fig. I-6. Layer thickness determinations based upon microwave data only. National Weather Service data provide the standard for comparison.

The temperature-sounding experiment, involving channels 3, 4, and 5, is also quite successful. Weighting functions for channels 3, 4, and 5 peak near altitudes 4, 11, and 18 km. A major concern has been whether the microwave temperature soundings would be perturbed by clouds. The only such perturbations that are evident are the small deflections of channel 3 which occur over the center of the ITC zone. These deflections of channel 3 are ~0-4°K and of short duration. No evidence now exists for such perturbations outside the tropics. There is little spatial variation of channels 3, 4, and 5 on a 100-mile scale; the scale size of the variations is much larger.

Figure I-6 shows plots of layer thicknesses inferred from channels 3, 4, and 5 for orbit 166. A 20-m thickness corresponds to ~1°K in the two lower layers, and to ~0.5°K in the upper layer. The 1000-500 mb thickness is compared with that generated by the National Weather Service for 1200Z, approximately 4 hours earlier. The difference never exceeds the equivalent of ~3°K despite the time difference and the

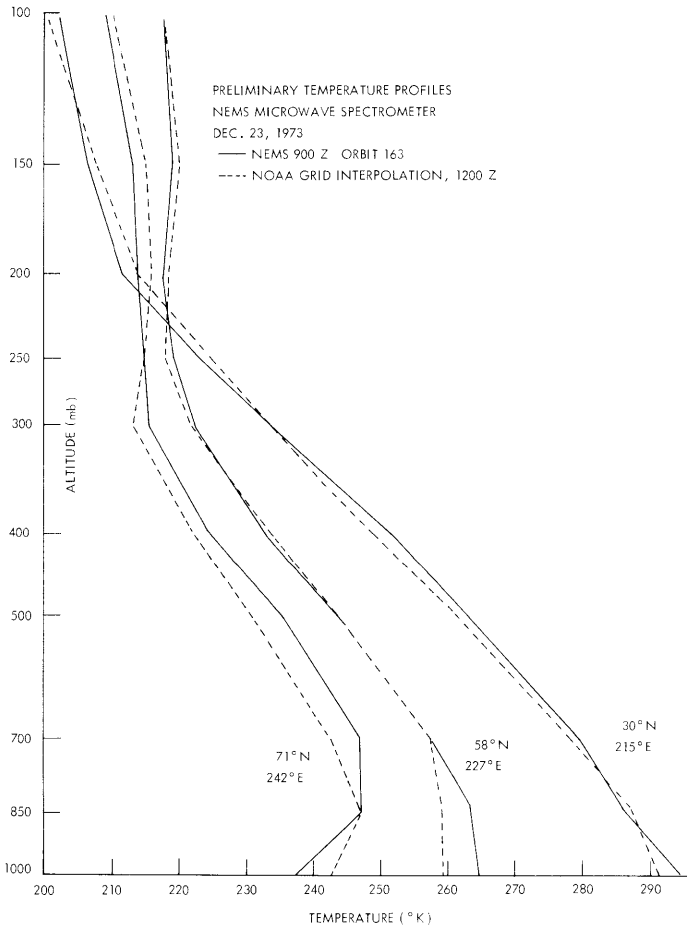

Fig. I-7. Preliminary temperature profiles determined from microwave data alone. The National Oceanic and Atmospheric Administration (NOAA) data provide the standard for comparison.

preliminary nature of these results. It is very interesting to note that the microwave data show the 1000-500 mb and 250-50 mb portions of the atmosphere between 20°N and 10°S to be the same within ~1°K peak-to-peak, which implies great accuracy for the NEMS measurements of temperature gradients. This accuracy may be sufficient to enable observation of tropical dynamics.

Figure I-7 shows 3 NEMS-inferred temperature profiles, together with the corresponding 1200Z NOAA grid interpolation. These results are quite reasonable, particularly because the calibration constants have not yet been fully revised by comparison of NEMS brightness temperatures with those calculated for coincident meteorological measurements.

C. MEASUREMENTS OF HIGH-J ATMOSPHERIC O_2 LINES FROM AIRCRAFT

National Aeronautics and Space Administration (Contract NAS1-10693)
California Institute of Technology (Contract 952568)

J. W. Waters, B. G. Anderson, K. F. Kunzi

During February and March, 1973, our 53-GHz radiometer-spectrometer system[1] for sensing upper stratospheric temperatures was flown on the NASA Convair 990 aircraft during the 1973 Joint US/USSR Bering Sea Experiment (BESEX). The overall objective of BESEX, which involves operation of an aircraft and a ship from each of these two countries in the Bering Sea area, is an international effort to evaluate microwave remote sensing for terrestrial applications. The scientific objectives of our experiment are measurements of (i) tropospheric opacity near 53 GHz, (ii) strength and spectral shape of atmospheric emission from high-J O_2 lines as observed at different altitudes and global locations, and (iii) upper stratospheric temperature variations above

Fig. I-8. 53-GHz radiometer-spectrometer system in operation on the NASA Convair 990 aircraft.

the flight path. The measurements from different altitudes should help explain the discrepancy between calculated and measured line strengths which we have previously observed from the ground.[1]

Figure I-8 shows the system in operation aboard the aircraft. The filter bank, computer system, teletype, and power supplies are installed in a standard double-bay equipment rack. The radiometer is mounted on top of the rack with a waveguide ~60 cm long connecting it to a horn antenna looking out through a 65° elevation observation port. The antenna of 10° beamwidth comes from a back-up model of the Nimbus-5 satellite Microwave Spectrometer Experiment (NEMS), and its linear electric polarization is parallel to the direction of flight. The 53-GHz system computer software was extended to improve the efficiency of observations during the flights, and an external

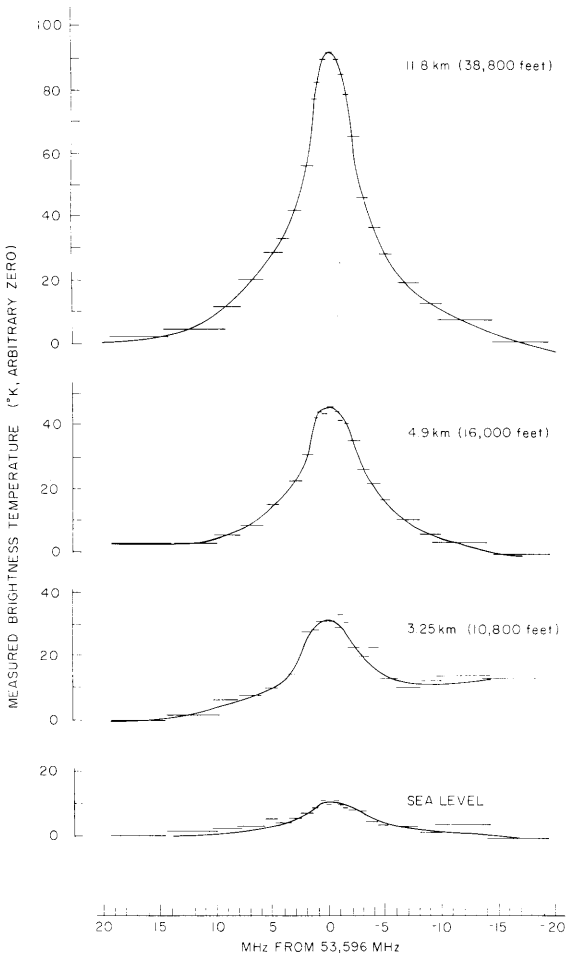

Fig. I-9.
Atmospheric emission by the 25_ O_2 line measured at various altitudes over Southwestern United States. Zenith angle of the observations is 25°, and the observation at 3.25 km is noisier than the others because of shorter integration time and no balance noise added to the radiometer. Horizontal bars indicate bandwidths of individual filters; uncertainty in the amplitude scale is approximately ±10%.

clock was added to enable automatic recording of the times of start and end of observation. Aircraft position, altitude, orientation, and other sensor data are obtained from the output of the aircraft data system.

By February 28, 1973 seven BESEX data flights have been completed: one over Southwestern United States, one from San Francisco to Alaska, and 5 over the Bering Sea. No problems have been encountered with the 53-GHz system. Figure I-9 shows measurements of the 25_ O_2 line taken at several altitudes during the first flight on February 8, 1973. The analysis of these and other measurements will be summarized in a subsequent report, and discussed in a journal publication.

We wish to thank J. C. Blinn III, H. C. Cross, D. C. Papa and E. V. Petersen for assistance with the installation of the instrument on the aircraft.

References

1. J. W. Waters, R. M. Paroskie, J. W. Barrett, D. C. Papa, and D. H. Staelin, "Radiometer System for Ground-Based Measurement of Stratospheric Temperatures," Quarterly Progress Report No. 107, Research Laboratory of Electronics, M.I.T., October 15, 1972, pp. 23-26.

D. NEUTRAL HYDROGEN ABSORPTION IN QUASI-STELLAR OBJECTS

National Science Foundation (Grant GP-21348A#2)

P. C. Crane, T. S. Giuffrida, J. H. Spencer, B. F. Burke

1. Introduction

We made a list of quasi-stellar objects (QSOs) with identified optical absorption lines, and then undertook a radio search for the Doppler-shifted neutral-hydrogen ground-state hyperfine transition (ν_o = 1420 MHz) at redshifts corresponding to the redshifts of the optical absorption. The observing frequencies, in the range 250-500 MHz, correspond to $z > 1.84$. In this report we review the observations and interpretation of the optical absorption lines. Because detection of the radio line depends on the optical depth of the line which depends upon the excitation temperature, the mechanisms that determine these parameters are discussed. Finally, we indicate the importance of this radio search, and describe our method of observation and our results.

2. Optical Absorption Lines

Quasi-stellar objects, the most distant and fastest-moving of extragalactic objects, were long unrecognized. It has been difficult to identify the lines in their spectra because they are extremely faint ($V \geq 17$) and because of the contributing factors of lack of understanding of the physical conditions in QSOs and of knowledge of the relation between observed and intrinsic wavelength scales. Nevertheless, in 1963, Schmidt identified 4 broad emission lines in the spectrum of 3C273, the brightest known QSO, which gave $z = \Delta\lambda/\lambda = 0.158$. Since then the emission redshifts of 250 QSOs have been measured. Among them is 4C05.34, the most distant object known ($z_{em} = 2.877$), which is ~5000 Mpc away.

Table I-1. Quasi-stellar objects with identified absorption lines.

QSO	z_{em}*	z_{abs}*	species observed	$n_H(cm^{-2})$	references	$T_{est}(10^4K)$
PHL 1194	0.299	0.283	MgII		7	0.7-2
PKS 151 -08	0.361	0.351	MgII		17	0.7-2
PKS 1229-02	0.388	0.395	MgII		32	0.7-2
PKS 0812+02	0.402	0.344	MgII		32	0.7-2
		0.384	MgII		32	0.7-2
PKS 1317-00	0.89	0.87	MgII		23	0.7-2
3C 309.1	0.905	0.889	MgII		1,17,20	0.7-2
BSO 1	1.241	1.241	CIV		25	4-20
3C 298	1.439	1.419	CIV		6	4-20
4C 17.46	1.449	1.439	CIII,CIV		22	4-20
3C 270.1	1.519	1.498	CIV		2	4-20
3C 205	1.534	1.538	CIV		20	4-20
Mk 132	1.75	1.73	Lα,CIV,SiIV		44	4-5
PKS 2146-13	1.800	1.785	CIV,SiIV		1,19	4-5
B 194	1.864	1.8366	Lα,NV,SiII,CIV		5	2-7
		1.8946	Lα,NV,SiIV,CII,CIV		5	2-7
RS 23	1.908	1.873	Lα,NV,CIV		9,19	7-20
PHL 1222	1.910	1.934	Lα		7	0-40
PHL 938	1.955	0.6128	FeII,MgII	$\gtrsim 10^{18}, 2\times10^{19}$	10,30,37,39,40	0.7-2
		1.9064	Lα,CIV,SiIII		12,30,38,39	4
PKS 0119-04	1.955	1.965	Lα,NV,SiIII,SiIV,CIII,CIV,SiII		32	4-7
3C 191	1.956	1.947	Lα,NV,SiII,SiIII,SiIV,CII,CIII,CIV	5×10^{20}	4,13,14,15,16,38	2-7
PHL 5200	1.981	1.8910	SiII,SiIV		5	3-4
		1.90-1.98	Lα,NV,SiIV,CIV		8,9,38,41	5-7
		1.9502	SiII,SiIV		5,8	3-4
PHL 1127	1.990	1.95	Lα		21	0-40
Ton 1530	2.051	1.8866	Lα,NV,SiII,CIV		30 see also 37	2-7
		1.9215	Lα,SiII,CIV		30	2-4
		1.9362	Lα,SiIV,CIV,Al II	2.2×10^{19}	30,31,39	2-4
		1.9798	Lα,CIV		30,31,39	4-20
		2.0553	Lα,CIV		39,40	4-20
BSO 11	2.084	2.028	Lα,NV,CIV		19	2-4
PKS 1116+12	2.118	1.947	Lα,CIV	$>10^{14}$	2,3,11,38	4-20
PKS 0237-23	2.228	1.3646	SiII,CIV,AlII,AlIII,FeII,MgII,AlII		36,39 †	2-4
		1.5132	SiII,SiIV,CII		36	2-3
		1.5958	CIV	7×10^{18}	39	4-20
		1.6564	SiII,SiIV,CIV,AlII	8×10^{18}	36,39	2-3
		1.6715	SiII,SiIV,CII,CIV,AlII,FeII		36,39	2-4
		1.6744	Lα,SiIV,CII,CIV		39	3-4
		1.9556	Lα,SiII,SiIII,SiIV,NI,NII,CIII,CII		34,35,38,39	2-3
		2.2017	Lα,SiIII,SiIV,NII,FeIII,TiIII,CI		33,34,35,36,39	3-4
4C 25.5	2.360	2.3683	Lα,SiIII,CIV		24	4
5C 2.56	2.3901	2.3674	Lα,NV,SiIV		18,19	5-7
PHL 957	2.69	2.0721	Lα,SiIII,SiIV,CII,NII,FeIII		28,29	3-4
		2.2065	Lα,SiIV,CII,NII,NV,OVI		28,29	5-7
		2.2259	Lα,Lβ,SiII,SiIII,SiIV,CII,FeII,SIII,OVI		28,29	2-3
		2.3099	Lα,Lβ,SiII,CII,AlII,OI	10^{20}	28,29, 43	0.6-2
		2.6624	Lα,Lβ,L ,SiIII,CIII,NII	10^{15}	28,29	1-4
4C 05.34	2.877	1.7758	SiII,SiIV,CII,CIV,AlII		27	2-4
		1.8593	SiII,SiIV,CII		27	2-3
		2.1819	Lα,SiII,SiIV,CII,FeII		27	2-3
		2.4743	Lα,SiIV,CIII,CIV,NII,NV,OVI		26,27	2-7
		2.5925	Lα,Lβ,SiIV,NII,NV,OVI		27	5-7
		2.7703	Lα,Lβ,Lγ,Lδ,Lε,SiIII,CII,CIII,CIV,FeII,FeIII		26,27	2-4
		2.8106	Lα,Lβ,Lγ,SiII,CIII,CIV,NV		26,27	2-7
		2.8751	Lα,Lβ,SiIII,SiIV,CIV,NV,OI,OVI,ArII		26,27	2-7

† see also 37,42

* (G. R. Burbidge and S. L. O'Dell, 1972, Ap. J., 178, 583)

References for Table I-1.

1. C. R. Lynds, Astrophys. J. 147, 837 (1967).
2. M. Schmidt, Astrophys. J. 144, 443 (1966).
3. C. R. Lynds and A. N. Stockton, Astrophys. J. 144, 446 (1966).
4. M. Grewing and T. Schmidt-Kaler, Z. Astrophys. 69, 247 (1968).
5. E. M. Burbidge, Astrophys. J. (Letters) 155, L43 (1969).
6. C. R. Lynds, S. J. Hill, K. Heere, and A. N. Stockton, Astrophys. J. 144, 1244 (1966).
7. E. M. Burbidge, Astrophys. J. (Letters) 154, L109 (1968).
8. E. M. Burbidge, Astrophys. J. (Letters) 152, L111 (1968).
9. J. D. Scargle, L. J. Caroff, and P. D. Noerdlinger, Astrophys. J. (Letters) 161, L115 (1970).
10. M. H. Demoulin and N. Doras, Astron. Astrophys. 4, 339 (1970).
11. J. N. Bahcall, B. A. Peterson, and C. M. Schmidt, Astrophys. J. 145, 369 (1966).
12. T. D. Kinman, Astrophys. J. 144, 1232 (1966).
13. A. N. Stockton and C. R. Lynds, Astrophys. J. 144, 451 (1966).
14. E. M. Burbidge, C. R. Lynds, and G. R. Burbidge, Astrophys. J. 144, 447 (1966).
15. E. M. Burbidge and C. R. Lynds, Astrophys. J. 147, 388 (1967).
16. J. N. Bahcall, W. L. W. Sargent, and M. Schmidt, Astrophys. J. (Letters) 149, L11 (1967).
17. E. M. Burbidge and T. D. Kinman, Astrophys. J. 145, 654 (1966).
18. E. M. Burbidge and P. A. Strittmatter, Astrophys. J. (Letters) 174, L57 (1972).
19. E. M. Burbidge, Astrophys. J. (Letters) 160, L33 (1970).
20. M. Schmidt, Astrophys. J. 151, 393 (1968).
21. A. Sandage and W. J. Luyten, Astrophys. J. 148, 767 (1967).
22. R. Lynds and D. Wills, Astrophys. J. (Letters) 153, L23 (1968).
23. J. G. Bolton, T. D. Kinman, and J. V. Wall, Astrophys. J. (Letters) 154, L105 (1968).
24. M. Schmidt and E. T. Olsen, Astron. J. 73, S117 (1968).
25. A. Sandage, Astrophys. J. 141, 1560 (1965).
26. C. R. Lynds, Astrophys. J. (Letters) 164, L73 (1971).
27. J. N. Bahcall and S. Goldsmith, Astrophys. J. 170, 17 (1971).
28. J. L. Lowrance, D. C. Morton, P. Zucchino, J. B. Oke, and M. Schmidt, Astrophys. J. 171, 233 (1972).
29. D. C. Morton and W. A. Morton, Astrophys. J. 174, 237 (1972).
30. J. N. Bahcall, P. S. Osmer, and M. Schmidt, Astrophys. J. (Letters) 156, L1 (1969).
31. W. A. Morton and D. C. Morton, Astrophys. J. 178, 607 (1972).
32. T. D. Kinman and E. M. Burbidge, Astrophys. J. (Letters) 148, L59 (1967).
33. H. C. Arp, J. G. Bolton, and T. D. Kinman, Astrophys. J. 147, 840 (1967).
34. E. M. Burbidge, Astrophys. J. 147, 845 (1967).
35. J. L. Greenstein and M. Schmidt, Astrophys. J. (Letters) 148, L13 (1967).
36. J. N. Bahcall, J. L. Greenstein, and W. L. W. Sargent, Astrophys. J. 153, 689 (1968).
37. J. N. Bahcall and U. Feldman, Astrophys. J. 161, 389 (1970).
38. G. Burbidge, Astrophys. J. 147, 851 (1967).
39. E. M. Burbidge, R. C. Lynds, and A. N. Stockton, Astrophys. J. 152, 1077 (1968).
40. Y. W. Tung Chan and E. M. Burbidge, Astrophys. J. 167, 213 (1971).
41. C. R. Lynds, Astrophys. J. 147, 396 (1967).
42. G. Grueff, Astrophys. Letters 4, 141 (1969).
43. E. A. Beaver, E. M. Burbidge, C. E. McIlwain, H. W. Epps, and P. A. Strittmatter, Astrophys. J. 178, 95 (1972).
44. W. L. W. Sargent, Astrophys. J. 173, 7 (1972).

An isolated, unidentified absorption line in 3C48 was observed in 1964. In 1966, Bahcall and Salpeter[1] discussed the probable absorption lines to be seen in quasars. Later that year several groups discovered the rich absorption-line spectrum of 3C191. Since then, as listed in Table I-1, 56 absorption-line systems have been identified in 29 QSOs. For each QSO Table I-1 gives its designation, $z_{emission}$ and $z_{absorption}$ according to Burbidge and O'Dell,[2] observed ionic species plus the Lyman series, published estimates of the column density of neutral hydrogen, references for line identifications, and estimates of kinetic temperature from the observed lines. In some QSOs a hundred lines have been observed but not all have been identified. At the other extreme, single, isolated lines such as are observed in 3C48 are unidentified; some single lines are on top of identified emission lines and thus are identified with the emission lines.

The nature of QSOs has been and is still hotly debated: Are they local, ejected by an explosive event in our galaxy, or are they cosmological objects and really at the great distances implied by their redshifts? Naturally, the origin of the absorption lines has helped fuel this debate. For example, the first identifications of absorption lines in QSOs with $z_{em} > 1.9$ were of similar sets of lines with $z_{abs} \approx 1.95$. From this very limited sample, some observers concluded that there is a "standard" absorption spectrum with a magic redshift of 1.95, which is an intrinsic property[3,4] of QSOs. They then concluded that the emission redshifts of QSOs are also intrinsic and, therefore, that they are local objects. The statistics, however, are consistent with a random distribution of absorption redshifts,[2] and so this last hypothesis is now not accepted.

Bahcall[5] has suggested two classifications of absorption lines (both of which may occur in the same QSO).

Class I

These broad lines are almost certainly associated with QSOs, since $z_{em} \approx z_{abs}$. Sometimes excited fine-structure lines are seen that must originate in a relatively dense medium or near a very intense radiation source. The fact that $V_{relative} \approx V_{dispersion}$ suggests that Class I lines and the broad emission lines may have the same origin. A typical example of a QSO with Class I lines is 3C191 (see Fig. I-10).

Class II

These very narrow lines exhibit large redshift differences ($\Delta z = z_{em} - z_{abs} > 0.1$), and show no lines from excited fine-structure states. They occur in QSOs such as PKS 0237-23 that exhibit multiple absorption redshifts (see Fig. I-11).

To explain the cosmological origin of multiple absorption redshifts it has been suggested that the absorption may be caused by intervening matter along the line of sight, such as clouds, galaxies, or, as Bahcall and Spitzer[6] have suggested, galactic halos.

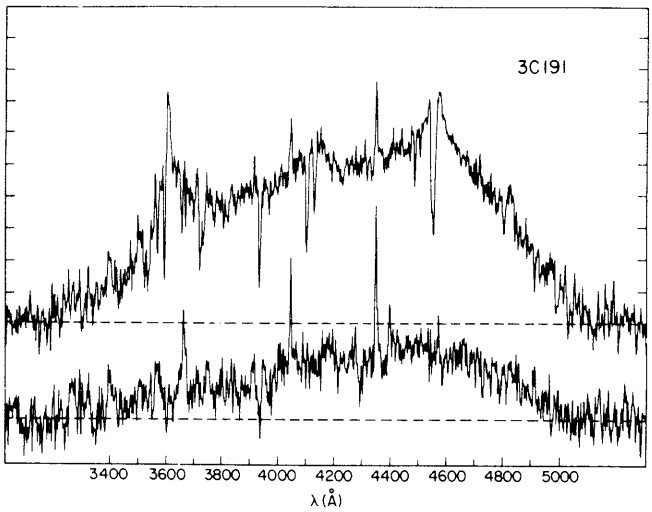

Fig. I-10. Density tracings of the spectrum of 3C191 and the spectrum of the nearby night sky. The strong emission lines in the spectrum of the night sky are due to the mercury line from city lights. [J. N. Bahcall, W. L. W. Sargent, and M. Schmidt, Astrophys. J. 149, L11 (1967), Figure 1, p. L12, reproduced with the permission of The Astrophysical Journal and The University of Chicago Press.]

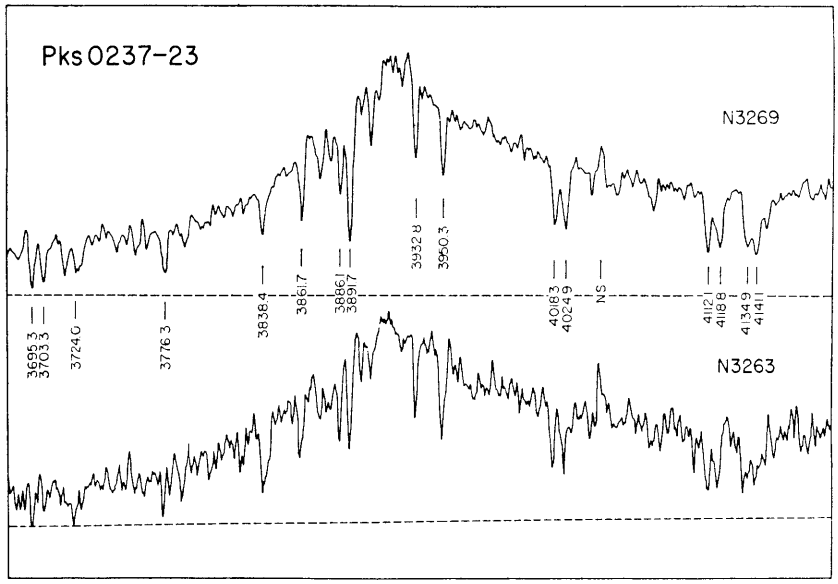

Fig. I-11. Density tracings of two 87 Å mm^{-1} spectrograms of PKS 0237-23. The illustrated region is dominated by the Lyman-α emission line with a redshift of z = 2.22. [J. N. Bahcall, J. L. Greenstein, and W. L. W. Sargent, Astrophys. J. 153, 689 (1968), Figure 1, p. 693, reproduced with the permission of The Astrophysical Journal and The University of Chicago Press.]

It has also been proposed by Rees[7] that the lines originate from discrete clouds of gas ejected at high velocity by the QSOs, perhaps, as suggested by Williams,[8] driven by radiation pressure acting on resonance lines, or that the lines originate in shells at very different gravitation potentials.

The cosmological hypothesis presents difficulties that are not insurmountable. Observational factors being equal, QSOs at the same z_{em} should serve equally well as probes of the intergalactic medium, but thus far only 4 (those most extensively studied) of the 48 QSOs with $z_{em} > 1.7$ have been observed to have multiple absorption redshifts. The distribution of absorption redshifts in these objects does appear to be more or less uniform as one would guess for cosmological origin. The local hypothesis has problems in explaining the extreme narrowness of the observed lines compared with their expansion velocities, and, in some cases, the observed degree of excitation. According to Lynds,[9] at the present time, the evidence seems to favor the local hypothesis.

3. Excitation of Neutral Hydrogen

The appearance of an absorption line in the spectrum of a bright source is determined by the equation of radiative transfer

$$\Delta T_A(\nu) = -T_A\left(1-e^{\tau_\nu}\right). \tag{1}$$

$\Delta T_A(\nu)$ is the line strength measured in °K of antenna temperature; T_A is the antenna temperature attributable to the continuum emission of the source, which is generally much greater than that of the line itself; and τ_ν is the frequency-dependent optical depth. T_A is directly proportional to the radiation flux incident on the antenna, but the absolute scale depends on the properties of the antenna. τ_ν is determined by the column density of absorbing atoms or ions, their excitation temperature T_S, and their velocity distribution. We shall now relate τ_ν to the atomic parameters and physical conditions of the neutral hydrogen; then we shall determine T_S for a range of conditions expected to prevail near a QSO.

First, let us consider the relations between the Einstein A and B coefficients:

$$I_{\nu_{21}} B_{12} = \frac{g_2}{g_1} B_{21} I_{\nu_{21}} \tag{2}$$

$$I_{\nu_{21}} B_{21} = \frac{A_{21}\lambda_{21}^3 I_{\nu_{21}}}{2hc}, \tag{3}$$

where $I_{\nu_{21}}$ is the specific intensity at the transition frequency ν_{21}, and g is the

statistical weight. Then the effective absorption coefficient (corrected for induced emission) is

$$\kappa_\nu = \frac{g_2}{g_1} \frac{c^2 A_{21}}{8\pi\nu^2} n_1 f(\nu)\left(1 - e^{-h\nu/kT_S}\right) \tag{4}$$

where T_S is the excitation temperature defined by

$$\frac{n_2}{n_1} \equiv \frac{g_2}{g_1} e^{-h\nu/kT_S}$$

and $f(\nu)$ is the probability that an atom can absorb a photon with frequency ν. At optical frequencies $h\nu \gg kT_S$ and the quantity in parentheses ≈ 1, while at radio frequencies $h\nu \ll kT_S$ and the same quantity $\approx h\nu/kT_S$. Thus, optical absorption is a direct measure of the number of atoms along the line of sight, since almost all are in the ground state. But in the radio range, absorption measures the ratio n_1/T_S. For the 21-cm transition of hydrogen $h\nu/k = 0.0681°$; therefore, $n_1/n_2 \approx 1/3$ and $n_1 \approx 3/4\ n_H$. Also, $A_{21} = 2.85 \times 10^{-15}\ s^{-1}$, and we find

$$\kappa_\nu = 2.58 \times 10^{-15}\ n_H f(\nu)/T_S. \tag{5}$$

The optical depth τ_ν is then the integral of κ_ν along the line of sight

$$\tau_\nu = \int_0^\ell \kappa_\nu\, d\ell. \tag{6}$$

The optical depth τ integrated across the line is given by

$$\Delta\nu\,\tau = 2.58 \times 10^{-15}\ N_H \frac{1}{T_S}, \tag{7}$$

where N_H is the column density of H I, and $\Delta\nu$ is the width of $f(\nu)$. Or, in terms of velocity (cm/s),

$$\Delta v\,\tau = 5.49 \times 10^{-14}\ N_H \frac{1}{T_S}. \tag{8}$$

In the case of optical transitions, $A_{21} \sim 10^{-8}\ s^{-1}$ and the frequency is greater by 10^6. Equations 4 and 6 show why hydrogen radio absorption is much more difficult to observe than optical absorption.

In the galaxy $T_S \sim T_K \sim 100°K$. The absorbing regions that we hope to observe, however, may be near the QSOs; if so, the intense radiation fields of the QSOs will

determine T_S. We shall show this by following the analyses of Field[10] and of Bahcall and Ekers.[11]

The 21-cm transition of hydrogen is between the two hyperfine states of the $1\ ^2S_{1/2}$ level of hydrogen, which differ only in the total spin angular momentum $\vec{F} = \vec{I} + \vec{S}$; $I = S = 1/2$, so that $F = 0$ or 1. The singlet $F = 0$ state ($g = 2F + 1$) lies 1420.405 MHz below the $F = 1$ triplet state. We use Boltzmann's law to define the spin (excitation) temperature even if thermodynamic equilibrium does not exist. In equilibrium, T_S will be determined by the relative total rates at which atoms enter and leave states 1 and 2. If we denote these rates P_{12}^T and P_{21}^T (and $T_* = h\nu_{21}/k$), then

$$n_1 P_{12}^T = n_2 P_{21}^T \tag{9}$$

or

$$\frac{P_{12}^T}{P_{21}^T} = \frac{n_2}{n_1}\frac{g_2}{g_1} \exp(-T_*/T_S) \approx 3(1-T_*/T_S). \tag{10}$$

The principal mechanisms that determine T_S are (i) particle collisions (kinetic energies of protons and electrons), (ii) direct excitation and de-excitation by absorption and emission of 21-cm photons (ambient 21-cm flux), and (iii) indirect excitation and de-excitation by absorption of ultraviolet photons leading to states that ultimately decay to the ground-state hyperfine levels (ambient Lyman flux). Mechanisms (ii) and (iii) are unusually important in the vicinity of QSOs. We shall first see how these mechanisms together determine T_S, and then look at each mechanism separately.

If we define the radiation temperature T_R as usual by

$$T_R \equiv \frac{\lambda_{21}^2}{2k} I_{21}, \tag{11}$$

then using the relations between the Einstein A and B coefficients, we find

$$P_{12}^R = 3A_{21} T_R/T_*, \tag{12}$$

$$P_{21}^R = A_{21}(1+T_R/T_*), \tag{13}$$

and

$$\frac{P_{12}^R}{P_{21}^R} \approx 3\left(1 - \frac{T_*}{T_R}\right). \tag{14}$$

We also define the kinetic temperature T_K and the Lyman-α temperature $T_{L\alpha}$.

$$\frac{P_{12}^c}{P_{21}^c} \equiv \frac{g_2}{g_1} \exp(-T_*/T_K) \cong 3\left(1 - \frac{T_*}{T_K}\right), \tag{15}$$

$$\frac{P_{12}^{L\alpha}}{P_{21}^{L\alpha}} \equiv \frac{g_2}{g_1} \exp(-T_*/T_{L\alpha}) \cong 3\left(1 - \frac{T_*}{T_{L\alpha}}\right). \tag{16}$$

Then

$$\frac{n_2}{n_1} = \frac{P_{12}^T}{P_{21}^T} = \frac{P_{12}^R + P_{12}^c + P_{12}^{L\alpha}}{P_{21}^R + P_{21}^c + P_{21}^{L\alpha}} \cong 3\left(1 - \frac{T_*}{T_S}\right)$$

$$= 3\,\frac{A_{21}T_R/T_* + (1-T_*/T_k)P_{21}^c + (1-T_*/T_{L\alpha})P_{21}^{L\alpha}}{A_{21}(1+T_R/T_*) + P_{21}^c + P_{21}^{L\alpha}} \tag{17}$$

or

$$1 - \frac{T_*}{T_S} = \frac{T_R/T_* + (1-T_*/T_k)P_{21}^c + (1-T_*/T_{L\alpha})P_{21}^{L\alpha}}{1 + T_R/T_* + P_{21}^c/A_{21} + P_{21}^{L\alpha}/A_{21}}, \tag{18}$$

$$\frac{T_*}{T_S} = \frac{1 + T_*P_{21}^c/T_kA_{21} + T_*P_{21}^{L\alpha}/T_{L\alpha}A_{21}}{1 + T_R/T_* + P_{21}^c/A_{21} + P_{21}^{L\alpha}/A_{21}}. \tag{19}$$

Finally, we obtain

$$\boxed{T_S = \frac{T_* + T_R + y_c T_K + y_{L\alpha} T_{L\alpha}}{1 + y_c + y_{L\alpha}}}, \tag{20}$$

where $y_c \equiv \frac{T_*}{T_K}\frac{P_{21}^c}{A_{21}}$ and $y_{L\alpha} \equiv \frac{T_*}{T_{L\alpha}}\frac{P_{21}^{L\alpha}}{A_{21}}$ are the normalized probabilities or "efficiencies."

Now let us examine the mechanisms individually.

Mechanism 1. The collision rates are dominated by collisions with other hydrogen atoms and free electrons, and are primarily attributable to the spin-exchange process, rather than the spin-flip process, which involves a magnetic dipole interaction. Bahcall and Ekers[11] give, without reference, the following expression for y_c.

$$y_c \sim 40\, n_{HI} T_{K,2}^{-0.8} + 10^3\, n_e T_{K,2}^{-1/2}(1+T_{K,2})^{-1/2}. \tag{21}$$

For the sake of estimation, we assume that $T_K = 10^4$°K, $n_{HI} = 10\ cm^{-3}$, and $n_e = 100\ cm^{-3}$ which give $y_c = 10^3$ and $y_c T_K = 10^7$°K.

Mechanism 2. If a QSO has a measured flux S_ν at $\nu = 1420.405/(1+z_{abs})$ MHz frequency and an emission redshift z_{em}, T_R is given by

$$T_R = \frac{\lambda^2}{2k} \frac{(1+z_{abs})}{4\pi} S_\nu \left(\frac{D}{r}\right)^2, \tag{22}$$

where $(1+z_{abs})$ corrects for the Doppler shift,[12] D is the luminosity distance of the QSO, so that for $q_o = 1$ and $H_o = 50$ km/s/Mpc,

$$D = 6000\, z_{em}\ \text{Mpc}, \tag{23}$$

and r is the distance of the absorbing medium, which is assumed to be near the QSO. We find

$$T_R = 4.3 \times 10^{13}\text{°K}\ \frac{(1+z_{abs})z_{em}^2}{r_{pc}^2} S_\nu\ (\text{f.u.}). \tag{24}$$

Mechanism 3. When we consider the effects of ultraviolet excitation, it is only necessary to consider Lyman-α radiation. This radiation has a very short mean-free path in hydrogen and still survives many collisions because splitting into two photons via a permitted transition to an intermediate state is not possible. We need only consider transitions between levels that can mix the hyperfine-level populations (see Fig. I-12 with relative intensities shown). Then

$$P_{12}^{L\alpha} = B_{13}\bar{I}_{\nu_{13}} \frac{A_{32}}{A_{32}+A_{31}} + B_{14}\bar{I}_{\nu_{14}} \frac{A_{42}}{A_{42}+A_{41}} \tag{25}$$

$$P_{21}^{L\alpha} = B_{23}\bar{I}_{\nu_{23}} \frac{A_{31}}{A_{32}+A_{31}} + B_{24}\bar{I}_{\nu_{24}} \frac{A_{41}}{A_{42}+A_{41}}. \tag{26}$$

Using the relations between the Einstein coefficients and the observed relative intensities, we find

$$P_{12}^{L\alpha} = \frac{B_{13}A_{32}}{A_{32}+A_{31}} \left(\frac{\lambda_{13}^3 \bar{I}_{\nu_{13}} + \lambda_{14}^3 \bar{I}_{\nu_{14}}}{\lambda_{13}^3} \right) \tag{27}$$

$$P_{21}^{L\alpha} = \frac{g_1}{g_2} \frac{B_{13}A_{32}}{A_{32} + A_{31}} \left(\frac{\lambda_{23}^3 \bar{I}_{\nu_{23}} + \lambda_{24}^3 \bar{I}_{\nu_{24}}}{\lambda_{23}^3} \right). \tag{28}$$

From the defining relation for $T_{L\alpha}$ we obtain

$$T_{L\alpha} = T_* \frac{\lambda_{23}^3 \bar{I}_{\nu_{23}} + \lambda_{24}^3 \bar{I}_{\nu_{24}}}{\lambda_{23}^3 \bar{I}_{\nu_{23}} + \lambda_{24}^3 \bar{I}_{\nu_{24}} - \lambda_{13}^3 \bar{I}_{\nu_{13}} - \lambda_{14}^3 \bar{I}_{\nu_{14}}}. \tag{29}$$

If $\bar{I}_\nu \propto \nu^\beta$ (where typically $-0.2 \geq \beta \geq -2$ for a QSO), then

$$T_{L\alpha} = \frac{h\nu_{23}}{(3-\beta)k} \cong 4(1-\beta/3) \times 10^4 \text{°K}. \tag{30}$$

(If, as seems appropriate for the interstellar medium, the shape of the spectrum

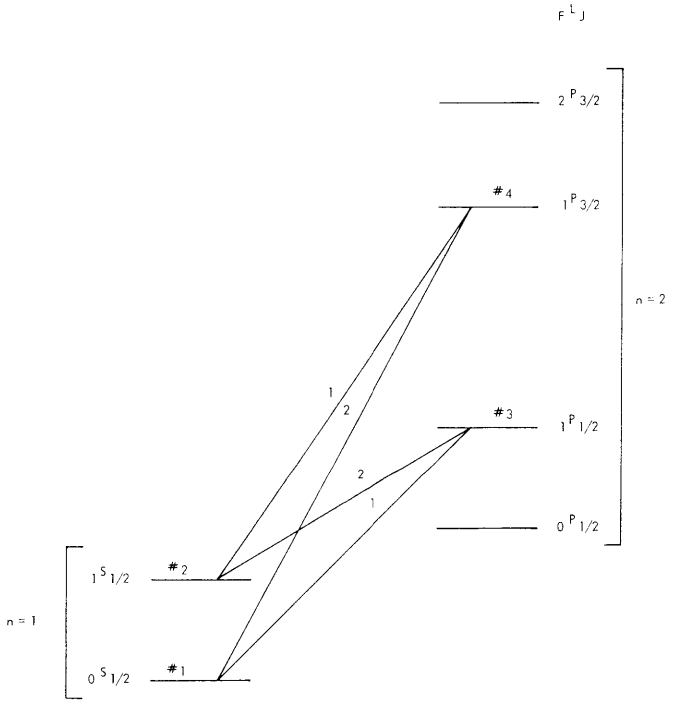

Fig. I-12.

Energy levels of the hydrogen atom contributing to the Lyman-α transition. Transitions that mix the hyperfine level populations and their relative intensities are indicated.

near the Lyman-α region is determined by the kinetic temperature of the absorbing atoms, $T_{L\alpha} = T_K$.) Also,

$$y_{L\alpha} T_{L\alpha} \cong \frac{\lambda_{23}^3 \bar{I}_{\nu_{23}}}{hc} \frac{A_{32}}{3A_{21}} T_*. \tag{31}$$

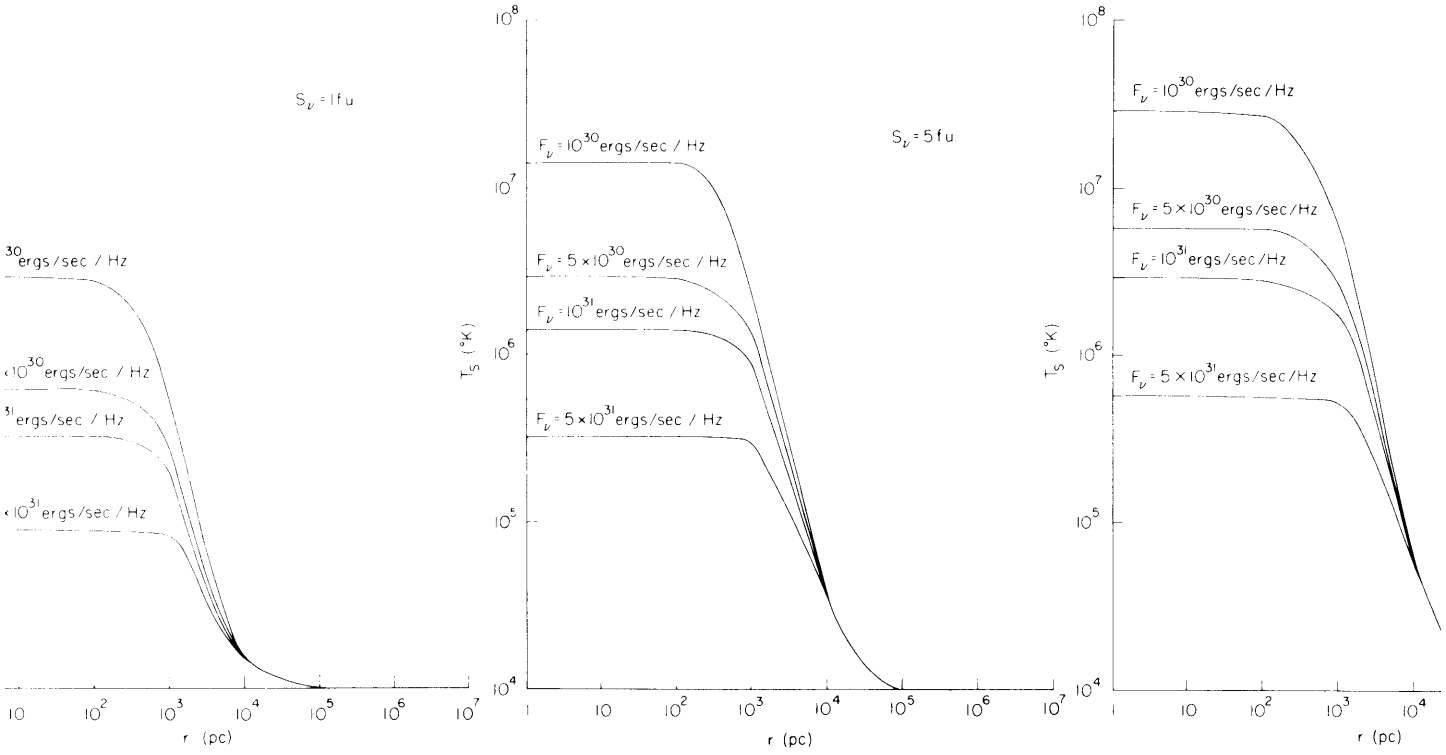

Fig. I-13. Dependence of the excitation temperature of neutral hydrogen on its distance from a quasi-stellar object for several values of S_ν and F_ν (under the assumption that $\delta = 0.25$, $\beta = -1$, $z_{abs} \cong z_{em} = 2$, $T_K = 10^4$° K, $n_{HI} = 10$ cm^{-3}, and $n_e = 10^3$ cm^{-3}).

If the QSO has intrinsic luminosity in the Lyman-α region F_ν ($\sim 5\times10^{30}$ ergs/s-Hz),[13] for $A_{32} = 5.4\times10^{8}\ s^{-1}$, Eq. 3 gives

$$y_{L\alpha}T_{L\alpha} = \frac{2.8\times10^{13}\,^{\circ}K}{r_{pc}^{2}}\left(\frac{\delta}{0.25}\right)\left(\frac{F_\nu}{5\times10^{30}\ \text{ergs/s}^{-1}\text{-Hz}^{-1}}\right)\left(\frac{1+z_{abs}}{1+z_{em}}\right), \qquad (32)$$

where δ is a geometric factor (0.25 for a spherical absorber) that determines the fraction of the absorber that is illuminated.

Figure I-13 shows graphically the spin temperature T_S as a function of r for different values of S_ν and F_ν. Figure I-13 confirms several conclusions that follow from Eqs. 21, 24, 30, and 32:

1. At large distances from a QSO the excitation temperature T_S is determined by the thermal equilibrium of the cloud.

2. Near a radio QSO ($S_\nu \sim 1$ f.u.) T_S is determined primarily by the radiation temperature weighted by its relative efficiency.

3. Near a radio-quiet QSO ($S_\nu \sim 0.01$ f.u.) T_S is determined by the flux in the Lyman-α region.

4. From Table I-1 we see that for typical values of n_H and T_K ($10^{19}\ cm^{-2}$ and $10^{4}\ ^{\circ}K$) determined from the optical observations and for $\Delta v = 100$ km/s, $\tau = 5.5\times10^{-6}$. If these conditions do prevail, then it will be difficult to detect neutral hydrogen absorption from such regions.

4. Radio Observations

a. Need for Radio Observations

The successful detection of the redshifted 21-cm line of neutral hydrogen in the spectra of QSOs would give direct checks on the correctness of the optically identified absorption redshifts; in fact, it would confirm the observational basis of our present knowledge about QSOs. Such detection would also improve our understanding of the physical conditions in the absorbing regions (for example, measurements of the velocity profiles and line strengths could indicate the location of the absorbing material, and furnish information about the cosmic abundances); it would also improve our knowledge of the physical laws and constants at large distances (for example, the ratio of the proton and electron masses).

For the conditions deduced from optical observations we cannot expect to detect neutral hydrogen absorption in the 21-cm line. With present resolution, however, optical data do not exclude the existence of very narrow lines (widths less than 100 kHz). The significance of a detection is so great that a search should be made. Several observers have looked at a limited number of objects,[14-17] and have been able to

Table I-2. Observational data and results.

Source	Z	Integration time (sec)	ΔT_{rms} (°K)	T_A (°K)	τ *	$N_{H/T}$ † $10^{19}/cm^2 °K$
B194	1.8946	6580	0.08	0.0	-	-
RS23	1.873	6080	0.09	0.1	∞	-
PHL1222	1.934	1920	0.22	1.9	<0.87	<15.8
PHL938	1.9064	1600	0.18	7.4	<0.13	< 2.4
PKS0119-04	1.965	2680	0.18	2.4	<0.48	< 8.7
3C191	1.947	2680	0.13	2.0	<0.38	< 6.9
PHL5200	1.8910	6820	0.09	6.8	<1.1	<20.0
PHL1127	1.95	3300	0.17	1.4	<0.94	<17.1
Ton1530	1.9362	3240	0.12	0.2	∞	-
	1.8866	3280	0.12	-4.5	?	?
BS011	2.028	6580	0.08	4.1	<3.5	<63.8
PKS1116+12	1.947	9840	0.10	4.3	<0.13	< 2.4
4C25.5	2.3683	2580	0.14	1.8	<0.49	< 8.9
PHL957	2.3099	1840	0.13	1.05	<0.97	<18.0
4C05.34	2.4743	5140	0.07	0.25	∞	-
	2.8751	2620	0.14	0.1	∞	-

* $\tau < \frac{5\Delta T_{rms}}{T_A}$

† Δv = 100 km/sec

obtain upper limits on τ of the order of 0.02-0.10.

b. Observations

Our observations were made January 5-11, 1973, using the 300-ft transit telescope of the National Radio Astronomy Observatory at Green Bank, West Virginia. We used the 250-500 MHz transistor front end and the Model III autocorrelator receiver, and observed in the total power mode. Finally, we reduced our data by using the T-Power off-line programs of NRAO.[18]

Our results are summarized in Table I-2, which lists sources, absorption redshift, total integration time, calculated rms temperature fluctuation, antenna temperature of the source, and when meaningful, an upper limit on τ ($= 5\ \Delta T_{rms}/T_A$) and the corresponding upper limit on N_H/T_S calculated from Eq. 8 for $\Delta v = 100$ km/s. Our present results do not place very restrictive upper limits on n_H/T_S. Our upper limits on n_H are typically in the range 10^{24}-10^{27} cm^{-2} for T_S in the range 10^4-10^7°K, which is at least four orders of magnitude greater than the few estimates from the available optical observations. Consequently, these observations are not very significant.

One problematical aspect of our results is the poor correlation between the observed antenna temperatures and the known radio properties ($S_\nu \leq 0.1$ f.u.) of the radio-quiet QSOs PHL 1222, PHL 938, PHL 1127, Ton 1530, and BSO 11.[19-22] On the other hand, the S_ν-T_A relation is well behaved for the radio sources PKS 0119-04, 3C191, PHL 5200, PSK 1116+12, 4C25.5, and 4C05.34. We believe this problem arises from our use of the autocorrelation receiver to measure T_A. One other complication, which occurred during the observations, was external RF interference from television and mobile transmissions. We deleted the poor records, but some unknown residual effects may possibly contribute to the problem.

We plan to repeat our present observations with better frequency resolution and with narrower bandwidths to avoid interference problems; so that we may be able to place much tighter limits on n_H/T_S. We also plan to extend our observations to other frequency ranges and to look at the very interesting object PKS 0237-23 which was not accessible with the 300-ft telescope.

References

1. J. N. Bahcall and E. E. Salpeter, Astrophys. J. 144, 847 (1966).
2. G. R. Burbidge and S. L. O'Dell, Astrophys. J. 178, 583 (1972).
3. G. R. Burbidge, Astrophys. J. 147, 851 (1967).
4. G. R. Burbidge and E. M. Burbidge, Astrophys. J. (Letters) 148, L112 (1967).
5. J. N. Bahcall, Astron. J. 76, 283 (1971).
6. J. N. Bahcall and L. Spitzer, Astrophys. J. (Letters) 156, L63 (1969).

7. M. J. Rees, Astrophys. J. (Letters) 160, L29 (1970).

8. R. E. Williams, Astrophys. J. 178, 105 (1972).

9. C. R. Lynds, "The Absorption-Line QSOs," in D. S. Evans (Ed.), External Galaxies and Quasi-Stellar Objects, Proc. International Astronomical Union Symposium No. 44, held in Uppsala, Sweden, 10-14 August 1970. (Springer-Verlag New York, Inc., New York, 1972), pp. 127-138.

10. G. B. Field, Proc. IRE 46, 240 (1958).

11. J. N. Bahcall and R. D. Ekers, Astrophys. J. 157, 1055 (1969).

12. S. Weinberg, Gravitation and Cosmology (John Wiley and Sons, Inc., New York, 1972).

13. E. J. Wampler, Astrophys. J. 153, 19 (1968).

14. W. L. H. Shuter and J. F. R. Gower, Nature 223, 1046 (1969).

15. C. Heiles and G. K. Miley, Astrophys. J. (Letters) 160, L83 (1970).

16. W. A. Dent, Astrophys. J. 165, 451 (1971).

17. G. A. Seielstad, B. Höglund, and E. Kollberg, Astrophys. J. 170, 219 (1971).

18. T. R. Cram, Internal Report No. 10, NRAO Computer Division, 1972.

19. K. I. Kellermann and I. I. K. Pauliny-Toth, Nature 212, 781 (1966).

20. K. R. Lang and Y. Terzian, Astrophys. J. (Letters) 158, L11 (1969).

21. B. Y. Mills and A. G. Little, Astrophys. Letters 6, 197 (1970).

22. J. F. C. Wardle and G. K. Miley, Astrophys. J. (Letters) 164, L119 (1971).